Remote Sensing of Cirrus Radiative Parameters during EUCREX'94. Case Study of 17 April 1994. Part II: Microphysical Models

HÉLÈNE CHEPFER AND GÉRARD BROGNIEZ

Laboratoire d'Optique Atmosphérique, Université des Sciences et Technologies de Lille, Villeneuve d'Ascq, France

LAURENT SAUVAGE AND PIERRE H. FLAMANT

Laboratoire de Météorologie Dynamique, Palaiseau, France

VINCENT TROUILLET AND JACQUES PELON

Service d'Aéronomie, Université de Paris VI, Paris, France

(Manuscript received 28 July 1997, in final form 30 April 1998)

ABSTRACT

In this paper, a quantitative analysis of in situ and radiative measurements concerning cirrus clouds is presented. These measurements were performed during the European Cloud and Radiative Experiment 1994 (EUCREX'94) as discussed in an earlier paper (Part I). The analyses are expressed in terms of cirrus microphysics structure. The complex microphysical structure of cirrus cloud is approximated by simple hexagonal monocrystalline particles (columns and plates) and by polycrystalline particles (randomized triadic Koch fractals of second generation) both arbitrarily oriented in space (3D). The authors have also considered hexagonal plates randomly oriented in horizontal planes with a tilted angle of 15° (2D). Radiative properties of cirrus cloud are analyzed, assuming that the cloud is composed of 3D ice crystals, by way of an adding–doubling code. For the hypothesis of 2D ice crystals, a modified successive order of scattering code has been used. The first order of scattering is calculated exactly using the scattering phase function of 2D crystals; for the higher orders, it is assumed that the same particles are 3D oriented. To explain the whole dataset, the most appropriate microphysics, in terms of radiative properties of cirrus clouds, is that of the 2D hexagonal plates whose aspect ratio (length divided by diameter) is 0.05.

1. Introduction

At mean and equatorial latitudes, cirrus clouds are detected in more than 50% of observations, and this probability is 25% in tropical areas (Woodbury and Mc Cormick 1986). Because of large spatial and temporal coverage and low temperatures due to their high location in the atmosphere, cirrus clouds have a major influence on the earth–ocean–atmosphere energy balance through their effects on the incoming solar radiation and on the outgoing infrared radiation (see among others Liou 1986; Ramanathan 1987; Ramanathan et al. 1989; Mitchell et al. 1989). As they are frequently optically thin, cirrus clouds take part in the greenhouse effect: (i) they partly reflect the incoming solar radiation, and (ii) they absorb the infrared radiation coming from the ground and emit it at a lower temperature, leading to higher tropospheric and earth surface temperatures. The climatic impact of cirrus clouds is now well recognized but not exactly determined (Hansen et al. 1984; Wetherald and Manabe 1988; Cess et al. 1990), because their optical properties are still not known very well. In order to understand the effects of cirrus clouds on the climate, the optical and radiative characteristics of these clouds have to be determined precisely. The radiative impact of a cirrus cloud depends on its temperature, its altitude, its optical depth, its heterogeneity, and, significantly, on its microphysical properties. Unlike water clouds, ice clouds are composed of crystals with an extremely large variability in shape and size (see among others Heymsfield 1975, 1977; Krupp 1991; Miloshevich and Heymsfield 1997). Until now, their parameterization in general circulation models (GCMs) still considers spherical particles. In order to correctly include the cirrus clouds in GCMs, our knowledge of the physical processes in cirrus cloud has to be improved.

Until recently, the observation and study of cirrus clouds were very difficult because of their high altitude

Corresponding author address: Dr. Gérard Brogniez, Laboratoire d'Optique Atmosphérique, Université des Sciences et Technologies de Lille, U.F.R. de Physique, 59655 Villeneuve d'Ascq, Cedex, France.
E-mail: gerard.brogniez@univ-lillel.fr

and their heterogeneity. Most aircraft were not able to fly high enough to observe cirrus clouds, and, in the case of semitransparent clouds, satellites were not able to distinguish a difference between the ground and the cirrus clouds. However, for about 15 years, intensive research has been carried out on cirrus clouds. Some new remote sensing methods using the multispectral satellite imagery were developed (Inoue 1985), and some intensive field experiments were possible using high-altitude flying aircraft. In 1986 and 1991 the First International Satellite Cloud Climatology Project Regional Experiment, held in the United States, was devoted to the study of midlatitude cirrus clouds (Mitchell and Arnott 1994; Arnott et al. 1994). This experiment was followed by the International Cirrus Experiment (ICE), held in September 1989 in northern Germany (Raschke and Rockwitz 1988; Raschke et al. 1990), and the European Cloud Radiation Experiment (EUCREX), which was held in Prestwick, Scotland, in September 1993, and in Brittany, France, in April 1994. For the study presented here, we focused our attention on the data collected during EUCREX'94.

EUCREX'94 was a three-aircraft and ground-based experiment (Sauvage et al. 1999, Part I of this paper). One of the aircraft was devoted to the study of low-level clouds; therefore, we have analyzed the data collected by two other aircrafts: the French Fokker 27 called ARAT (Avion de Recherches Atmosphériques et de Télédétection) operated by the Institut National des Sciences de l'Univers and the German Falcon operated by the Deutsche forschungsanstalt für Luft und Raumfahrt. During this experiment, four cases of cirrus clouds were studied. For the present work, we have analyzed data collected during two of these missions done on 17 April and corresponding to the same cirrus bank: mission 4 in the morning, and mission 5 in the afternoon. The cirrus bank was located between 7- and 11-km altitude, and the ARAT was flying below it at an altitude of about 5 km, whereas the Falcon was above or inside the cirrus cloud. The ARAT was carrying an upward-viewing lidar called LEANDRE (Lidar Embarqué pour l'étude des Aérosols, Nuage, Dynamique, Rayonnement et Espèces minoritaires) (Pelon et al. 1990) that operated at a wavelength of 532 nm, an upward-looking infrared radiometer Barnes precision radiation thermometer (PRT-5), and a Polarization and Directionality of the Earth's Reflectances (POLDER) downward-looking instrument operated by the Laboratoire d'Optique Atmosphérique. This instrument provides multidirectional radiance measurements in the visible and the near-infrared range (Deschamps et al. 1994). The Falcon was also fitted with a microphysical forward scattering spectrometer probe (FSSP) and an Optical Array Probe-Cloud (OAP-2D2-C) manufactured by Particles Measuring System (PMS Inc., Boulder, CO), which are operated by the Gesellschaft für Kernenergieverwertung in Schiffbau und Schiffahrt Research Center (Geesthacht) and a downward-looking POLDER instrument.

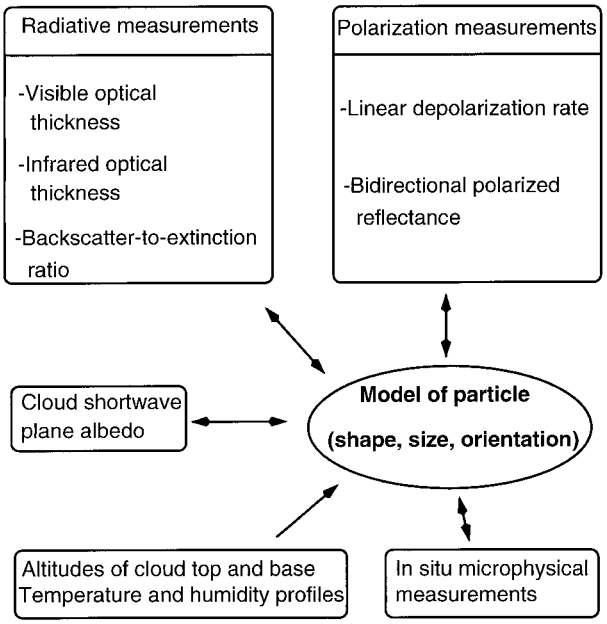

FIG. 1. Diagram of airborne measurements collected during EUCREX'94.

The FSSP probe allowed us to detect particles whose radius ranges between 3 and 45 μm, whereas the 2D-C probe detects crystals whose size ranges between 25 and 800 μm. The two aircrafts were also fitted with instruments to measure upward and downward fluxes (Eppley devices). National Oceanic and Atmospheric Administration/Advanced Very High Resolution Radiometer (NOAA/AVHRR) data were also analyzed. The detailed presentation of these instruments and the data analysis are presented in Part I of this paper.

The optical properties of cirrus clouds are strongly controlled by their microphysical properties and the goal of this work is to find a microphysical model capable of incorporating all the observations collected during these two flights (Fig. 1). In section 2, we recall definitions of measurements that will be compared with various simulations. To assess the sensitivity of the results to the shape of ice cloud particles, we present (in section 3) different ideal shapes of ice crystals in cirrus cloud: polycrystalline particles randomly oriented in space (Macke et al. 1996), and monocrystalline hexagonal particles randomly oriented in space (Brogniez 1988) or randomly oriented in the horizontal plane (Brogniez et al. 1992). In section 4, we present radiative transfer codes that are able to take into account Rayleigh scattering, atmospheric aerosols, and earth surface albedo. An adding–doubling code (De Hann et al. 1986) is considered for ice crystals randomly oriented in space, and a successive order of scattering code (Deuzé et al. 1988b) is adapted for the case of horizontally oriented ice crystals. The different types of ice particles are introduced in these radiative transfer codes to simulate the cirrus radiative properties deduced from measure-

TABLE 1. Scalar and polarization parameters measured during EUCREX'94.

Scalar parameters	Polarization parameters
Shortwave cloud optical thickness (lidar)	Backscattering linear depolarization ratio (lidar)
Backscattered to extinction ratio (lidar)	
Reflectance (AVHRR)	
Bidirectional total reflectance (POLDER)	Bidirectional polarized reflectances (POLDER)
Infrared emissivity (satellite and airborne radiometer)	
Cloud plane albedo (pyranometers)	

ments, and comparisons between each type of measurements and simulations are presented in section 5.

2. Data definitions

Polarization measurements (lidar linear backscattered depolarization and POLDER polarized reflectances) analyzed simultaneously can give us information on the shape of cirrus ice crystals. The backscattered signal lidar profiles show the vertical heterogeneities in the cloud and give the cloud geometrical properties: altitude, geometrical thickness, and horizontal extent. Cloud temperature, pressure, and relative humidity are given by probes mounted on-board the Falcon. Some in situ microphysical measurements, collected by the 2D-C and the FSSP PMS probes, give information on ice crystals size and concentration, and on the cirrus cloud ice water content (IWC). Optical thicknesses in shortwave and infrared ranges are given, respectively, by the lidar and by the PRT-5.

All the different measurements described above lead to the derivation of cloud optical parameters. Some of them are very sensitive to scattering processes in the cloud and, consequently, to the cirrus microphysical properties. These optical parameters are classified in scalar (section 2a) and polarization (section 2b) parameters and summarized in Table 1.

a. Scalar parameters

The shortwave optical thickness δ is deduced from the backscattered lidar signal profile $\beta(\pi)$ (Platt 1973; Platt et al. 1987).

The backscattering phase function $P(\pi)$ is deduced from the backscattered to extinction ratio k deduced from lidar measurements (Platt 1973; Platt et al. 1987):

$$k = \frac{P(\pi)}{4\pi} = \frac{\beta(\pi)}{\alpha_{\text{ext}}}, \tag{1}$$

where α_{ext} is the volume extinction coefficient.

The bidirectional cloud total reflectance $\rho(\theta_s, \varphi_s; \theta_v, \varphi_v)$ is deduced from airborne POLDER measurements collected above the cirrus cloud (Deschamps et al. 1994):

$$\rho(\theta_s, \varphi_s; \theta_v, \varphi_v) = \frac{\pi L(\theta_s, \varphi_s; \theta_v, \varphi_v)}{E_s \cos\theta_s}. \tag{2}$$

In this equation, E_s is the irradiance at the top of the atmosphere integrated through the given channel, $L(\theta_s, \varphi_s; \theta_v, \varphi_v)$ is the upward radiance scattered by the cloudy atmosphere, (θ_s, φ_s) are the zenithal and the azimuthal solar angles, and (θ_v, φ_v) are the zenithal and the azimuthal viewing angles.

The cloud total reflectance is measured with AVHRR (channel 1) in one viewing direction.

The emissivity $\varepsilon^{\downarrow}$ is deduced from the airborne infrared radiometer measurements collected below the cloud (Allen 1971), and the emissivity $\varepsilon^{\uparrow}$ is deduced from AVHRR measurements collected above the cloud.

The upward and downward shortwave fluxes above the cirrus cloud ($F^{\uparrow}_{\text{top}}$ and $F^{\uparrow}_{\text{top}}$) have been measured by pyranometers, and they allow the determination of the cloud plane albedo following the method worked out by Saunders et al. (1992):

$$a = \frac{F^{\uparrow}_{\text{top}}}{F^{\downarrow}_{\text{top}}}. \tag{3}$$

b. Polarization parameters

The backscattering linear depolarization ratio Δ_p is measured by the lidar (Sassen 1991):

$$\Delta_p = \frac{I_r}{I_\ell} \tag{4}$$

where I_ℓ and I_r are the backscattered intensities polarized, respectively, in the same direction as the incident laser beam and in the perpendicular direction.

The cirrus cloud bidirectional polarized reflectance $\rho_p(\theta_s, \varphi_s; \theta_v, \varphi_v)$ is deduced from POLDER measurements (Goloub et al. 1994):

$$\rho_p(\theta_s, \varphi_s; \theta_v, \varphi_v) = \frac{\pi L_p(\theta_s, \varphi_s; \theta_v, \varphi_v)}{E_s \cos\theta_s} \tag{5}$$

with

$$L_p(\theta_s, \varphi_s; \theta_v, \varphi_v) = (Q^2_{\text{SC}} + U^2_{\text{SC}} + V^2_{\text{SC}})^{1/2}, \tag{6}$$

where Q_{sc} U_{sc}, and V_{sc} are the Stokes parameters (van de Hulst 1981) of the upward scattered light above the cirrus cloud in the viewing direction (θ_v, φ_v) by reference to the solar incident direction (θ_s, φ_s).

Each kind of measurement will be compared to simulations one by one (sections 3 and 4), in order to determine one (or several) microphysical model(s) able to simultaneously fit the complete dataset.

3. Optical properties of ice crystals

This section is devoted to the presentation of optical properties of ideal shapes of cirrus ice crystals: mono-

crystalline particles (hexagonal columns or plates) randomly oriented in space or in the horizontal plane, and polycrystalline particles randomly oriented in space. We have compared elements of the scattering matrix, in particular single scattering phase functions and degrees of linear polarizations, which are necessary to simulate the observations of the intensity and the state of polarization of the scattered light. In this work, we also consider spherical particles whose optical properties were computed with Mie theory (Mie 1908).

a. Randomly oriented particles

Due to their symmetrical properties, the scattering matrix for a collection of hexagonal ice crystals or polycrystalline particles randomly oriented in space has only six independent elements P_{ij} (van de Hulst 1981). Stokes parameters (I_{sc}, Q_{sc}, U_{sc}, V_{sc}) of a beam of light scattered once by this type of particle in the scattering direction Θ are deduced from the incident parameters (I_i, Q_i, U_i, V_i) as follows:

$$\begin{pmatrix} I_{SC} \\ Q_{SC} \\ U_{SC} \\ V_{SC} \end{pmatrix} = \begin{pmatrix} P_{11}(\Theta) & P_{12}(\Theta) & 0 & 0 \\ P_{12}(\Theta) & P_{22}(\Theta) & 0 & 0 \\ 0 & 0 & P_{33}(\Theta) & P_{34}(\Theta) \\ 0 & 0 & -P_{34}(\Theta) & P_{44}(\Theta) \end{pmatrix} \begin{pmatrix} I_i \\ Q_i \\ U_i \\ V_i \end{pmatrix}. \tag{7}$$

For monocrystalline hexagonal columns and plates (Wendling et al. 1979; Cai and Liou 1982; Brogniez 1988; Takano and Liou 1989a) and for polycrystalline particles (Macke et al. 1996), this scattering matrix is obtained by ray-tracing calculations enhanced with Fraunhofer diffraction calculations. The phase function used in this paper was calculated with the code of Brogniez (1988). These results are consistent with those of Takano and Liou (1989a), which have been used to good effect by a number of researchers (i.e., Minnis et al. 1993). Shapes of hexagonal ice crystals are defined by their length L and their radius R, or by the aspect ratio $Q = L/2R$ and the radius R_v of a sphere of identical volume. Due to the ray-tracing method, elements of the scattering matrix are obtained in little boxes (typically $\Delta\Theta = 0.25°$) around a given scattering angle Θ. These calculations are only valid in the geometrical optic approximation (i.e., radius R_v greater than 15 μm). These elements are presented in Fig. 2 as a function of the scattering angle Θ, for polycrystalline particles, hexagonal columns with $Q = 2.5$, hexagonal compact particles with $Q = 1$, and hexagonal plates with $Q = 0.05$ and $Q = 0.1$, each of these crystals having a volume of a sphere of radius $R_v = 20$ μm. Due to the complex structure of polycrystalline particles, the six elements $P_{ij}(\Theta)$ of the matrix have a very smooth behavior compared to the elements relative to plates and columns. The influence of small ice crystals is not considered in this paper, it will be discussed in the part III of this series.

For scattering angles ranging between 60° and 110°, values of $P_{12}(\Theta)$ show an opposite slope for plates and for other types of crystal (positive slope for plates, and negative for columns and polycristalline particles). As the element $P_{12}(\Theta)$ is predominant in simulations of polarized light, the measurements collected between 60° and 110° of scattering angle allows discrimination between the hexagonal plates and the other shapes of particles.

In the case of randomly oriented particles, the backscattering linear depolarization ratio can be expressed, in the single scattering approximation, as a function of elements $P_{11}(\pi)$ and $P_{22}(\pi)$ (Sassen and Knight 1994):

$$\Delta_p = \frac{P_{11}(\pi) - P_{22}(\pi)}{P_{11}(\pi) + P_{22}(\pi)}. \tag{8}$$

Since values of $P_{11}(\pi)$ and $P_{22}(\pi)$ depend on ice crystal shape (Fig. 2), the backscattering linear depolarization ratio will obviously depend on this shape. For spherical particles, $P_{11}(\Theta) = P_{22}(\Theta)$ and $P_{33}(\Theta) = P_{44}(\Theta)$ (van de Hulst 1981), therefore the backscattering linear depolarization ratio Δ_p is equal to zero [see Eq. (8)]. Consequently, lidar measurements of Δ_p are signatures of the nonsphericity for ice crystals in the cirrus cloud, and they can give information on the ice crystal shape composing the cirrus cloud. Note that the uncertainty that remains is due to the fact that the ray-tracing caculations do not allow us to know exactly the value of these elements in backscattering (i.e., at $\Theta = \pi$). We can only assess the mean value in the nearest box from $\Theta = \pi$. In the same order of approximation, the backscatter-to-extinction lidar ratio will be compared to the mean value of the single scattering phase function in the nearest box from $\Theta = \pi$.

b. Horizontally oriented particles

In the case of horizontally oriented particles, the scattering medium is optically nonisotropic. We focused on the scattering phase function $P_{11}^{+}(\theta_s, \theta_v, \varphi_v)$. This element, computed with the ray-tracing method, depends on the incident zenith angle θ_s of the incoming beam of light, and on the direction of the scattered beam, that is, the viewing zenith angle θ_v and the azimuth viewing angle φ_v relative to the azimuth φ_s of the incident beam.

To approximately simulate the conditions in which horizontally oriented ice crystals in cirrus clouds fall wobbling (Platt 1978; Mc Dowell 1979; Rockwitz 1989), we considered hexagonal plates randomly oriented in the horizontal plane with oscillations of 15° amplitude. This amplitude has been chosen somewhat arbitrarily, since no exact data are available on oscillations of cirrus ice crystals during their falls. Figure 3 shows an example of a diagram of the scattering phase function $P_{11}^{+}(\theta_s, \theta_v, \varphi_v)$ above and below the horizon (Figs. 3a and 3b, respectively). These results correspond to hexagonal plates with an aspect ratio $Q = 0.05$ and a solar zenith angle θ_s equal to 38°. The downward

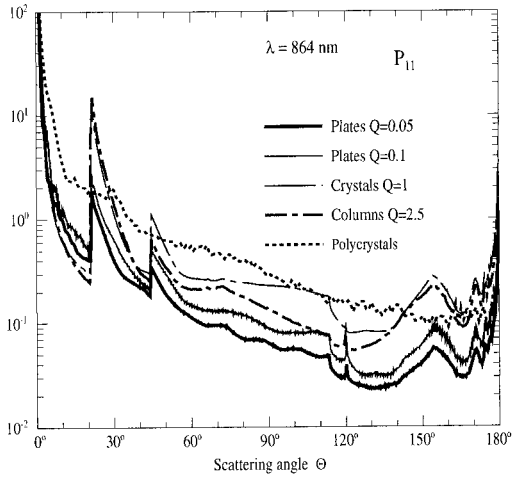

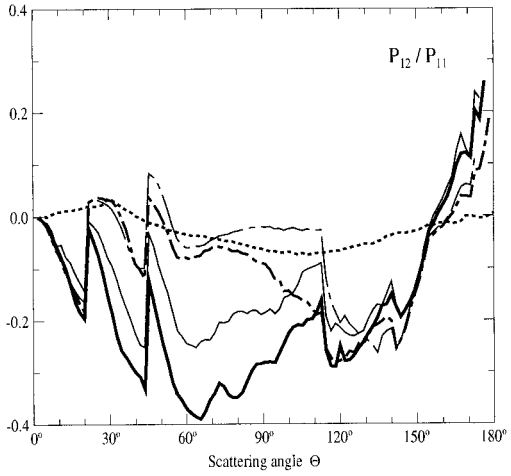

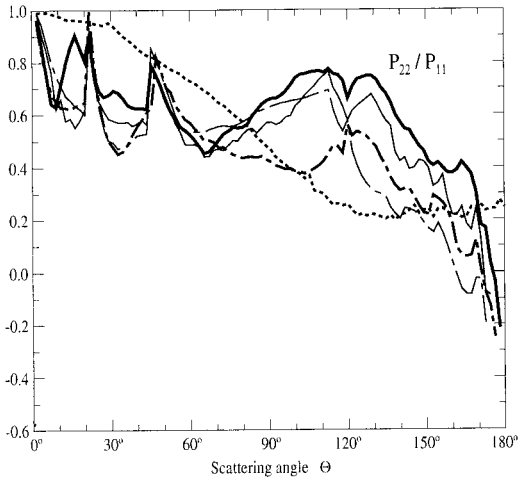

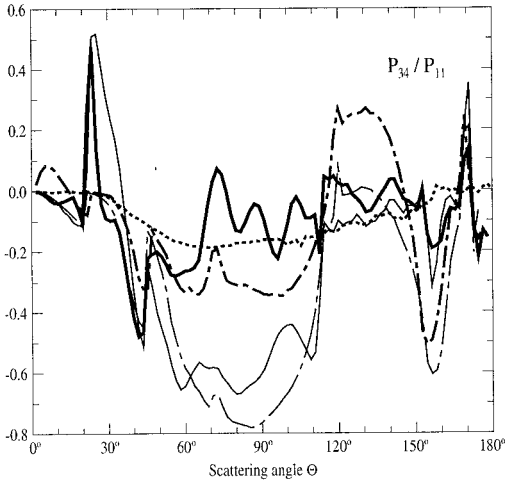

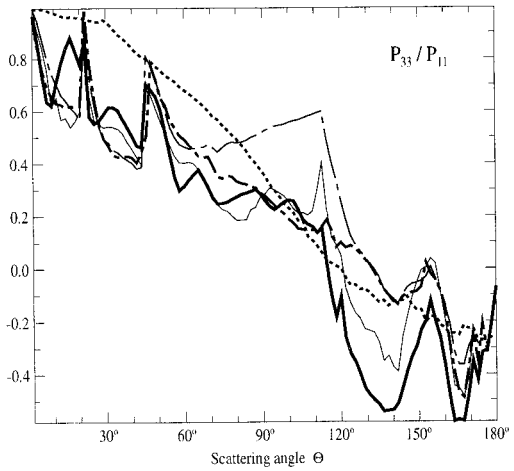

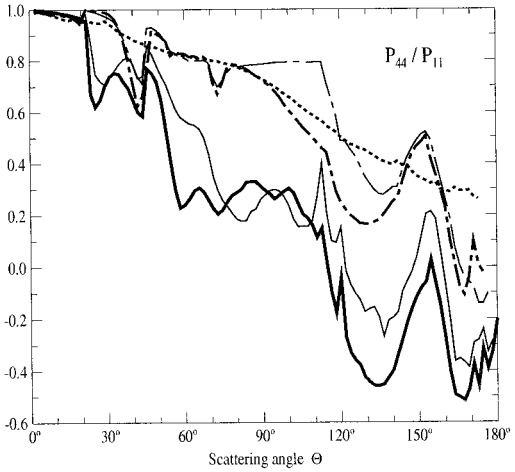

scattered field (Fig. 3b) shows an important forward scattering and diffraction peak, whereas the upward scattered field (Fig. 3a) shows a hot spot in the solar principal plane corresponding to the solar specular reflection at the zenithal viewing angle $\theta_v = \theta_s$. Obviously, the position of the specular reflection and the behavior of the scattering phase function depend on the solar zenith angle.

Moreover, the width and the intensity of both the specular reflection and the forward peak are functions of oscillation amplitude; the larger the amplitude of the oscillations is, the wider and less intense the hot spot and the forward peak are, because more energy is scattered outside the forward and the specular reflection directions. In the same way, characteristics of the hot spot and the forward peak depend on the aspect ratio Q and the size R_v of the crystal.

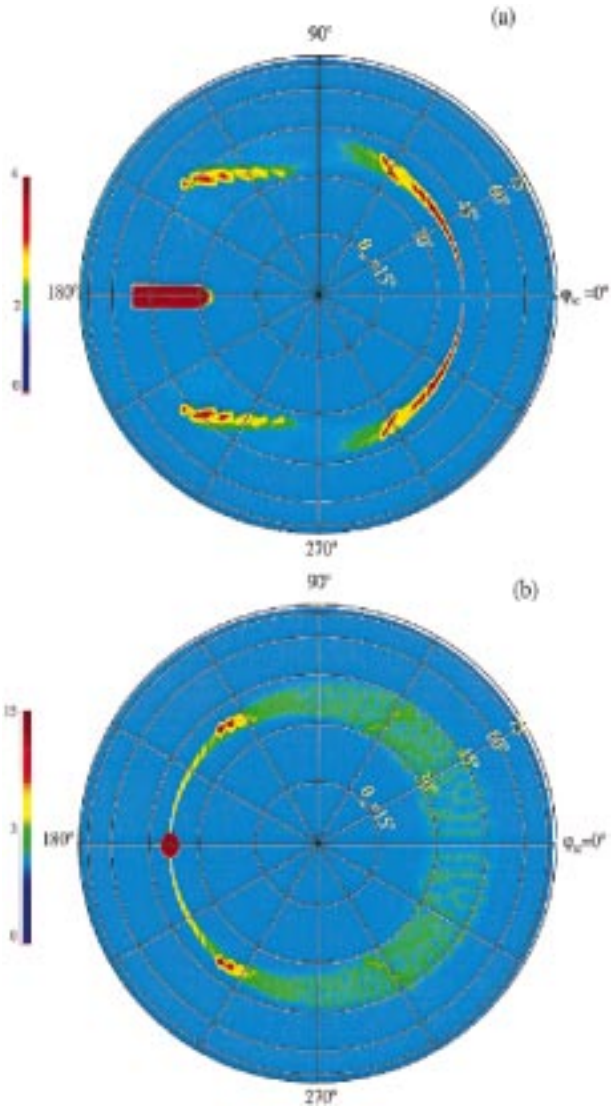

FIG. 3. Scattering phase function for hexagonal ice plate with an aspect ratio $Q = 0.05$ horizontally oriented with a tilted angle of 15°, and the solar zenith angle equal to 38°. (a) The scattering phase function in the upward direction; (b) the downward direction. Concentric circles are for constant θ_v. The angle between a radius and the 180°–0° axis is the azimuth viewing angle φ_v.

4. Radiative properties of cirrus clouds

a. Randomly oriented particles

An adding–doubling code developed by De Haan et al. (1986) was used to simulate radiative transfer in the whole atmosphere. This code took into account surface albedo, aerosols in the atmosphere, Rayleigh scattering, and cirrus cloud. This model was developed on the assumption that the atmosphere is divided in horizontal homogeneous plane-parallel layers. Each layer is divided in several sublayers, each one of them having an optical depth of 10^{-5}. Single scattering is calculated in one sublayer; the optical depth of the sublayer is then doubled, and doubled again, until the optical thickness reaches the value that corresponds to the initial atmospheric layer. Another homogeneous layer is put on the first one, and the contributions of the two layers are added. We considered a first layer composed of gaseous molecules and tropospheric aerosols. A second layer, located above the first one, is only composed of ice crystals and gaseous molecules, since the presence of tropospheric aerosols is negligible at the altitude of the cirrus cloud. In the following paragraphs we describe the way in which we defined these two layers.

1) CLEAR SKY CONDITIONS

In a first step, we had to simulate clear sky conditions in order to isolate the contribution of the cirrus cloud. The contribution of Rayleigh scattering is well known and can easily be taken into account. Tropospheric aerosol albedo is deduced from clear sky POLDER measurements, that is, bidirectional total reflectances measured at the two closed wavelengths (650 nm and 440 nm) following the method developed by Deuzé et al. (1988a).

This method is based on the assumption of single scattering, which allows us to write the aerosol total reflectance $\rho(\lambda, \Theta)$, for the wavelength λ, as follows:

$$\rho(\lambda, \Theta) = \frac{\delta(\lambda) P^a(\Theta)}{4 \cos\theta_s \cos\theta_v}, \tag{9}$$

←

FIG. 2. The six elements of the scattering matrix vs the scattering angle for a collection of polycrystalline particles and hexagonal monocrystalline particles (columns and plates) randomly oriented in space.

where Θ is the scattering angle and $P^a(\Theta)$ the aerosol single scattering phase function. Aerosol optical thickness $\delta(\lambda)$ is assumed to follow the Angström law:

$$\delta(\lambda) = \delta_o \lambda^{-\alpha}, \tag{10}$$

where α is the Angström coefficient and the constant δ_o is the aerosol optical thickness at the wavelength $\lambda = 1$ μm. The Angström law implies a Junge power law for the aerosols size distribution:

$$n(r) = Cr^{-\alpha-3}, \tag{11}$$

where $n(r)$ is the number of aerosol particles per volume unit with radii ranging between r and $r + dr$, and C is a normalizing coefficient.

Assuming that the aerosol scattering phase function is the same at 440 and 650 nm, and using measurements of bidirectional total reflectances at these two wavelengths, the Angström coefficient α is deduced (in our case $\alpha = 2$). In order to retrieve measurements in clear sky conditions, the bidirectional total reflectances are computed using the adding–doubling code. The parameters used to describe the atmosphere in the adding–doubling radiative transfer code are the following: Aerosols with an optical depth of 0.025 at 864 nm (the wavelength at which numerical simulation of cirrus clouds reflectances were computed). The optical properties of aerosols are computed with the Mie theory following the size distribution described above [Eq. (11)]. We have then considered one homogeneous layer of aerosols with an optical thickness equal to 0.025. In the radiative transfer code, this homogeneous layer has been subdivided in 2500 sublayers, each one of them having an optical thickness of 10^{-5} (De Haan et al. 1986); the single scattering is computed in each of the sublayers. Since we performed measurements above the ocean, we have to introduce a value of sea surface albedo in the adding–doubling code as boundary conditions. A suitable value of sea surface albedo in the shortwave range is 3% (Slingo and Schrecker 1982)

These results constitute the first homogeneous layer of aerosols in the adding–doubling code. Note that the three independent elements of the scattering phase matrix corresponding to the aerosols, considered as spherical and computed with Mie theory, have been developed in generalized spherical functions before being introduced in the radiative transfer code.

2) Cloudy conditions

The second layer corresponds to the cirrus cloud layer, and it is located above the first layer of aerosols. Again, the adding–doubling code is used to compute radiative transfer, and this second layer composed of cloud particles is divided in to several sublayers; each one has an optical thickness of 10^{-5} and the single scattering is computed in each sublayer. The second layer is located above the first one and is composed of ice crystals. As cirrus ice crystals are assumed to be prismatic particles randomly oriented in space, the diagonal elements of the scattering phase matrix present a sharp intense forward peak, which has to be truncated before being developed in generalized spherical functions. Hence, the scattering phase function $P_{11}(\Theta)$ is truncated betweeen 0° and 10° of scattering angle Θ, and the truncated scattering phase function $P^*_{11}(\Theta)$ is renormalized. Obviously, optical parameters (single scattering albedo, extinction coefficient, optical thickness) must be adapted to the truncated scattering phase function $P^*_{11}(\Theta)$ (Lenoble 1993), and the truncation has to be applied to the five other elements of the scattering matrix, to be coherent with the scattering phase function. For instance, the element $P_{22}(\Theta)$ becomes the truncated element $P^*_{22}(\Theta)$, such as

$$P^*_{22}(\theta) = \frac{P^*_{11}(\Theta)}{P_{11}(\Theta)} P_{22}(\Theta). \tag{12}$$

Elements of the scattering matrix and optical properties relative to the different types of randomly oriented prismatic ice particles and to the spherical particles were successively introduced in the adding–doubling code in order to calculate the Stokes vector (I_{sc}, Q_{sc}, U_{sc}, V_{sc}) of the emergent light at the top and the bottom of the cirrus cloud. Upward and downward integrated fluxes at the top and at the bottom of the cloud are deduced from the emergent Stokes vector. Also, bidirectional total and polarized reflectances can be deduced from the Stokes vector of the emergent light at the top of the cirrus cloud following Eqs. (2), (5), and (6). Calculated fluxes allow simulation of the cloud plane albedo using Eq. (3).

b. Horizontally oriented prismatic particles

A successive order of scattering code has been developed by Deuzé et al. (1988b) for spheres or randomly oriented prismatic particles. In this code, the atmosphere is separated in horizontal plane-parallel layers. The first order of scattering is calculated inside each layer, which is assumed to be homogeneous. Upward and downward radiance fields are calculated at each level, adding all the contributions of lower layers for the upward radiance field, and all the contributions of higher layers for the downward radiance field. The second order of scattering is calculated for each layer using the first order of scattering field as the new source of incident light. After addition of other layers' contributions, the third order of scattering is applied to these new fields. This process is repeated until the emergent light at the top of the atmosphere is small enough to be negligible. This code gives the radiance field and the integrated upward flux at the top of the atmosphere as outputs.

We have adapted this code to the case of horizontally oriented particles: The first order of scattering is calculated exactly using the scattering phase function $P^+_{11}(\theta_s, \theta_v, \varphi_v)$ of horizontally oriented ice crystals. For higher orders of scattering, we assume that the same

particle (i.e., same shape and size) is randomly oriented in space and follows the scattering phase function $P_{11}(\Theta)$. The use of randomly oriented scattering phase function $P_{11}(\Theta)$ for orders of scattering higher than one obviously constitutes an approximation, but the results will give a good idea of what could be obtained with rigorous modeling for horizontally oriented particles.

Hence, on the one hand, the first order of scattering gives a radiance field $I_1(\delta;\ \theta_v,\ \varphi_v)$ at each level of the atmosphere located at the optical thickness δ. This radiance field is developed in Fourier series as follows:

$$I_P(\delta,\ \theta_v) = \frac{\int_0^{2\pi} I_P(\delta;\ \theta_v,\ \varphi_v)\cos(p\varphi_v)\,d\varphi_v}{(2 - \Delta_{op})\pi}, \quad (13)$$

where the intensity terms $I_P(\delta,\ \theta_v)$ correspond to the order p of the development. These terms are calculated until the maximum order $p_{max} = 50$, which is a value high enough to correctly restitute the radiance field $I_1(\delta;\ \theta_v,\ \varphi_v)$. Here, φ_v is the azimuthal viewing angle and Δ_{op} is the Dirac function (unity for $p = 0$ and zero for $p \neq 0$). On the other hand, the truncated scattering phase function $P_{11}^*(\Theta)$ relative to the randomly oriented particles is developed in Legendre polynomial $P^\ell(\Theta)$, for each scattering angle Θ:

$$P_{11}^*(\Theta) = \sum_{\ell=0}^{\infty} \beta_\ell P^\ell(\Theta), \quad (14)$$

where β_ℓ is the Legendre coeffient of order ℓ. The maximum order of development ℓ_{max} is chosen to allow for a correct restitution of scattering phase function $P_{11}^*(\Theta)$. The Legendre coefficients are then applied to the first-order intensity values $I_P(\delta,\ \theta_v)$ considered as new sources for the calculation of the second order of scattering. Third and higher orders of scattering are computed with these Legendre coefficients until the contribution of the last order of scattering is small enough to be negligible.

Hence, these radiative transfer calculations, for clouds composed of crystals horizontally oriented in space, were used to compute scalar parameters measured during EUCREX'94 such as bidirectional total reflectances and cloud plane albedo. But none of the polarization parameters for cirrus cloud composed of horizontally oriented ice crystals were simulated. Indeed, our approximated successive order of scattering code developed for horizontally oriented ice crystals is not able to compute polarization. As far as we know, there are currently no radiative transfer codes able to compute polarization in the literature.

5. Analysis of satellite measurements

a. Particle size of cirrus clouds by satellite remote sensing

We have used the method developed first by Inoue (1985) and more recently by Giraud et al. (1997) to derive cirrus cloud particle size. This method relies on the important difference in the relationship between brightness temperatures for the channel 4 (10.3–11.3 μm) and channel 5 (11.5–12.5 μm) AVHRR data, and the microphysical properties of semitransparent cirrus cloud. In the nonscattering approximation, the absorption coefficient ratio, $\eta = \sigma_5^{abs}/\sigma_4^{abs}$ in the two channels, is the key parameter indicative of the size of cloud particles. In the hypothesis of spherical particles with a size distribution assumed to be a Gamma function, the effective radius of such spheres can be adjusted in order to obtain the measured value of the coefficient ratio η.

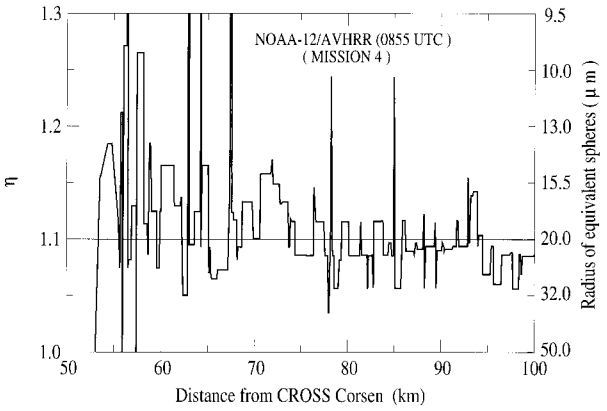

FIG. 4. Values of η deduced from AVHRR measurements (0855 UTC 17 April 1994, mission 4) corresponding to the densest part of the cloud, as a function of distance from Centre de Recherche d'Observation, de Secours et de Sauvetage (CROSS Corsen).

For satellite remote sensing, among the AVHRR data of 0855 UTC 17 April, we have considered the pixels coincident with aircraft measurements during mission 4. Considering each AVHRR pixel totally clear or totally cloudy, the values of η deduced from the pixels corresponding to the densest part of the cloud studied by the aircraft are reported in Fig. 4 with radius of equivalent spherical particles. Figure 4 displays a mean value of η equal to 1.1, corresponding to an effective radius of 20 μm for equivalent spheres. It is important to notice here that this value is self-consistent with the effective radius value deduced by in situ measurements (Part I of this paper), although neither the in situ measurements nor the AVHRR measurements allow us to obtain any information on the shape and the orientation of cirrus ice crystals.

b. Cirrus cloud asymmetry factor

The determination of the asymmetry factor g for cirrus ice crystals is fundamental to derive cirrus radiative properties. A value of the asymmetry factor of particles composing the observed cirrus cloud is derived using shortwave reflectances and infrared emittances following the method proposed by Wielicki et al. (1990).

We used the normalized AVHRR reflectances collected in channel 1 (0.58–0.68 μm), and emittances de-

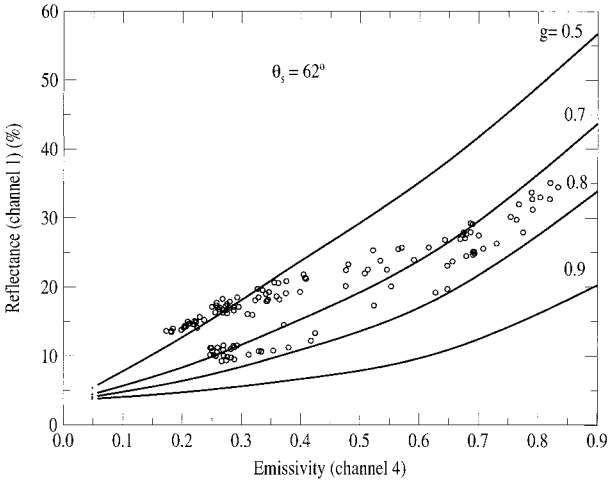

FIG. 5. AVHRR reflectances (in channel 1) as a function of AVHRR infrared emissivity (channel 4) corresponding to aircraft tracks of mission 4. The angles of the viewing direction are $\theta_v = 1.6°$ and $\varphi_s - \varphi_v = 182°$. Radiative transfer simulation using Henyey–Greenstein scattering phase function with asymmetry factor ranging between 0.5 and 0.9.

rived from brightness temperatures measured in channel 4 during mission 4. Theoretical reflectances are computed using an adding–doubling code (De Haan et al. 1986). In these simulations, the clear sky albedo is of the order of 5%, and the atmosphere is composed of a cirrus cloud layer for which crystal optical properties are described with Henyey–Greenstein scattering functions. Values of directional reflectances have been computed for asymmetry factors ranging between 0.5 and 0.9, and shortwave optical thickness of cirrus cloud δ_{SW} varies between 0.1 and 15. The infrared optical thickness δ_{IR} is deduced from δ_{SW} following the large particle approximation $\delta_{SW}/\delta_{IR} = 2$. We have considered the pixels corresponding to the aircraft track. For these pixels, the mean solar zenith angle is $\theta_s = 62°$ and the viewing direction is referred to by the mean angles $\theta_v = 1.6°$ and $\varphi_s - \varphi_v = 182°$ (θ_v is the zenithal viewing angle, and $\varphi_s - \varphi_v$ is the difference between solar and viewing azimuthal angles). Simulations and measurements are plotted in Fig. 5. Reflectances and emittances are well correlated, but all the data cannot be simulated with a single value of the asymmetry factor. Indeed, for the optically thin parts of the cloud, the measurements seem to be better simulated with asymmetry factors ranging between 0.5 and 0.8, whereas for the thicker parts of the cloud, the Henyey–Greenstein scattering functions with asymmetry factors ranging between 0.7 and 0.8 seem to be more adapted to fit the measurements.

6. Analysis of aircraft measurements

This section is devoted to the comparison of cirrus cloud radiative properties derived, respectively, from measurements and from the different microphysical models presented in the previous section. These comparisons allow us to determine the model that gives the best fit of the measurements and to check if a unique model is able to satisfy all the observations. We will have to keep in mind that hereafter in this paper, the model of particles horizontally oriented in space will only be considered to reproduce scalar parameters and not to retrieve polarized parameters (section 4b). Measurements were collected during flights 4 and 5 of the EUCREX experiment (Part I of this paper). In the following study, measurements were only taken into account when the aircraft were flying above, inside, and below the largest and the most homogeneous part of the cirrus cloud in order to justify the plane-parallel hypothesis that was considered for the simulations. These sequences correspond to a solar zenith angle θ_s of the order of 55° during mission 4 (leg F3), and a solar zenith angle of the order of 38° during mission 5 (leg F1).

a. Polarization measurements

Backscattering linear depolarization ratios, acquired by the lidar along leg A1 of mission 4, are presented in Fig. 6 as a function of altitude and distance. These values, corrected from the molecular depolarization, range between 0% and 35%. In the densest part of the cloud, which is located at distances ranging between 50 and 100 km, the backscattering linear depolarization ratio ranges between 15% and 20%. These linear depolarization ratio values cannot be explained by the spherical particles for which the value is equal to 0%. The linear depolarization ratio has been calculated for different shapes of randomly oriented particles in the single scattering approximation. Due to the sharp forward scattering peak and the narrow viewing angle of the lidar telescope, a photon that is received by the telescope has a high probability of having been forward scattered several times and only backscattered once. In fact, the forward scattering is mainly due to the diffraction effect, which does not have any incidence on the polarization, whereas the single backscattering changes the state of light polarization. This is why the single scattering approximation can be applied to the models of the lidar depolarization. The results of linear backscattering depolarization ratio calculations are presented in Fig. 7 as a function of the aspect ratio Q for hexagonal monocrystals. We have also reported the results obtained for polycrystals. Results show a maximum value of 86% for hexagonal plates ($Q = 0.2$), while columns ($Q = 20$) reach the lower value of 55%, and polycrystalline particles an intermediate value of 58%. Hence, the measured values (15%–20%) cannot be explained by microphysical models considered here.

Bidirectional polarized reflectances were measured along leg F3 during mission 4. POLDER data were selected when the aircraft was flying 1.5 km above the cloud top, over the most homogeneous part of the cloud. For this part of the cloud, at 0912 UTC, the solar zenith

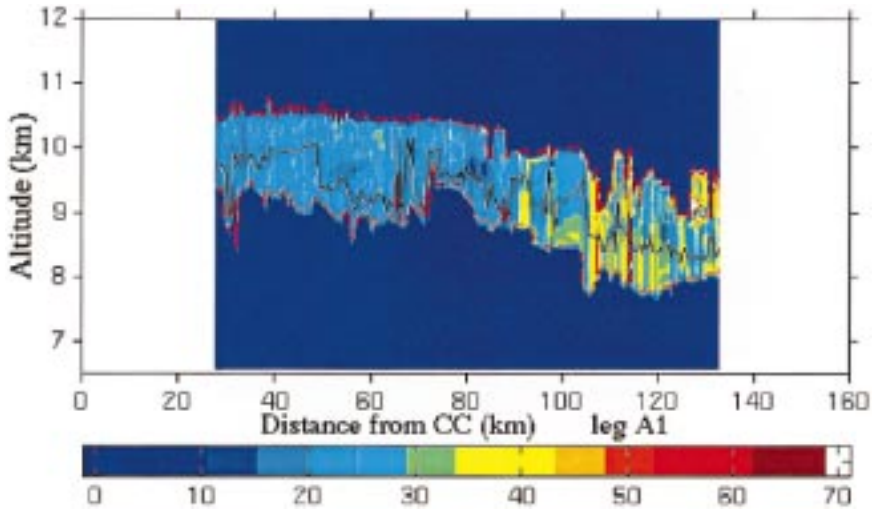

FIG. 6. Linear backscattering depolarization ratio obtained by the lidar LEANDRE along the leg A1 during the mission 4. The densest part of the cloud was located between 50 and 100 km from CROSS Corsen (CC)

angle θ_s is equal to 55.3°. The measurements of the bidirectional polarized reflectances in the solar principal plane, defined by $\varphi_v = 0°$, are presented in Fig. 8 as a function of the scattering angle Θ, and compared to the different randomly oriented particle models presented before. We can clearly see that in all the cases, the spherical particles cannot satisfy the observations. The best fit is obtained for monocrystalline hexagonal plates: aspect ratio $Q = 0.05$ associated with a cloud optical thickness δ equal to 1, or aspect ratio $Q = 0.1$ associated with a cloud optical thickness δ equal to 7. It is interesting to note that only hexagonal plates can explain the measurements, but with an important variation of cloud optical thickness depending on the aspect ratio value. We observe a difference between the shapes of particles. The most evident difference concerns the scattering angles ranging between 80° and 110°, which correspond to the opposite slope that was noticed in the behavior of the element $P_{12}(\Theta)$ of the scattering matrix (section 3a). Another example of measurements collected during mission 5 is presented in Fig. 9. In this case, corresponding to 1322 UTC, the solar zenith angle q_s is equal

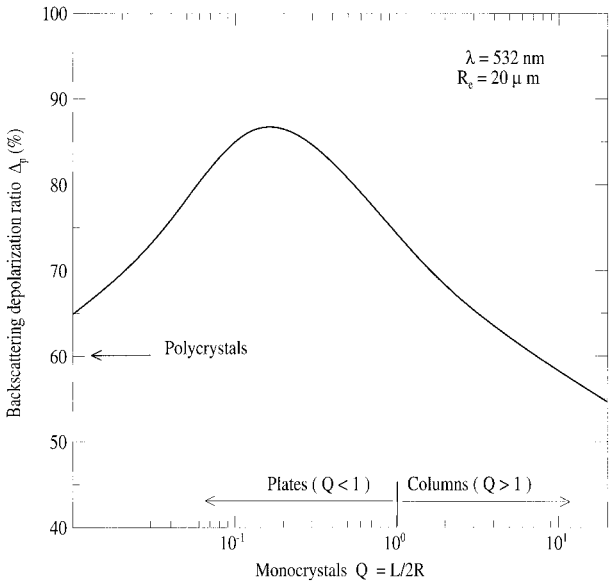

FIG. 7. Linear backscattering depolarization ratio calculations as a function of the aspect ratio $Q = L/2R$ of monocrystalline hexagonal particle randomly oriented in space. We have also reported the value obtained for polycrystalline particles.

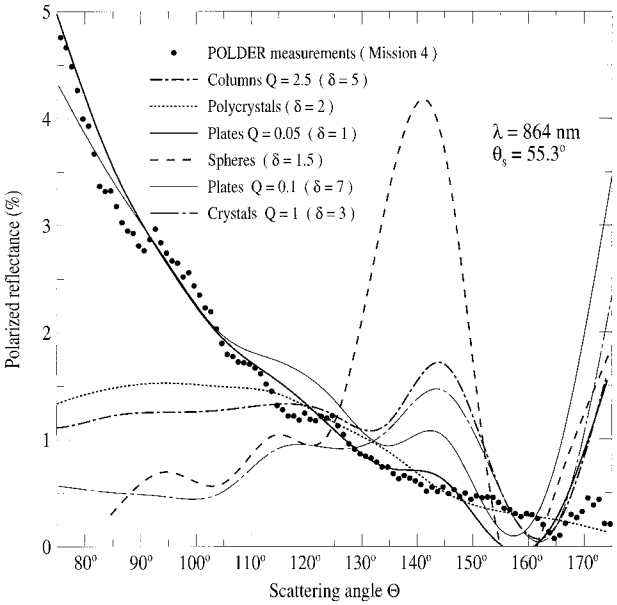

FIG. 8. Comparison of measurements of polarized reflectance obtained by POLDER during mission 4 in the solar principal plane and modeling with different crystal shapes.

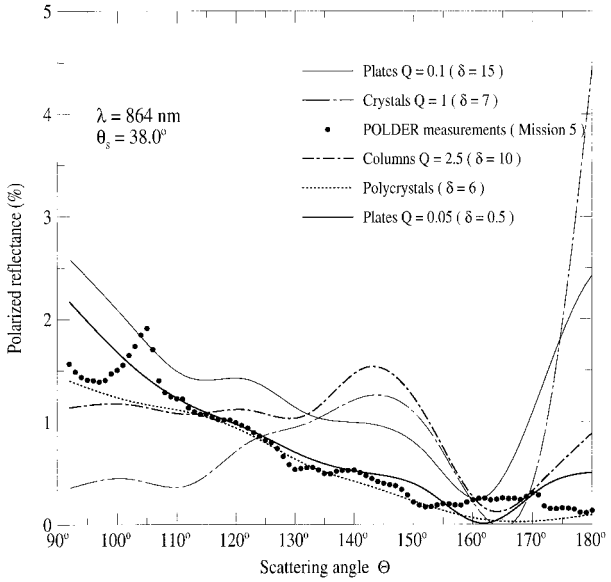

FIG. 9. Same as Fig. 8 but for mission 5.

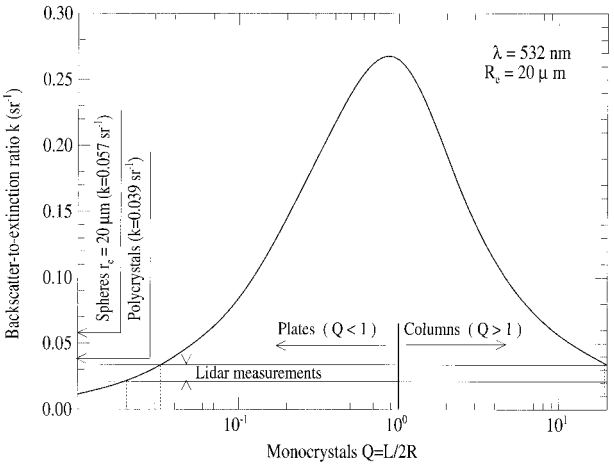

FIG. 10. Results of backscattered coefficient calculations as a function of the aspect ratio Q of monocrystalline hexagonal particles randomly oriented in space. We have also reported the value obtained for spheres and polycrystalline particles.

to 38.0°, and the observed scattering angles in the solar principal plane range between 90° and 180°. In this case, the observations seem to be better fitted with polycrystalline particles, but this model is not really satisfactory because it does not allow us to reproduce the specular reflection peak at $\Theta = 104°$.

b. Directional radiative measurements

Backscattered signal profiles measured by the lidar were collected during mission 4 along leg A1. They were corrected for multiple scattering effect (see Part I), and the relative uncertainty of these measurements ranges between 5% and 15%, depending on the absolute value of the backscattered signal. We focused our attention on the densest part of the cloud: it had to be consistent with previous polarization measurement analyses. For this sequence, the backscattered to extinction ratio is of the order of 0.024 sr^{-1}. Different models of randomly oriented prismatic particles are compared to these measurements. The backscattered to extinction ratio is plotted in Fig. 10 as a function of the aspect ratio Q of hexagonal particles. We have also reported the backscattered to extinction ratio corresponding to polycrystals and spherical particles. The measured value can be explained by randomly oriented plates with low values of Q ranging between 0.02 and 0.03. With respect to horizontally oriented ice crystals, we have to consider that the airborne lidar that collected data was looking at about 20° from the zenith. Mishchenko et al. (1997) has shown that, in that configuration, the backscattered signal is lower for horizontally oriented ice crystals than for randomly oriented ones. Although these calculations do not concern hexagonal plates, but ice cylindrical disks, and even if they do not take into account oscillations, they express a tendency. In our case, the backscattered to extinction ratio calculated for 3D hexagonal plates is of the order of 0.05, whereas the measured ratio is half that value. Following Mishchenko et al.'s results, these differences could be due to the horizontal orientation of the ice crystals.

The calculations for cirrus cloud optical thickness δ at 532 nm have been obtained by integration of the backscattered lidar signal profiles. Multiple scattering effects have been taken into account in the determination of δ (Part I). Values of δ along leg A1 are plotted in Fig. 11 as a function of the distance from the Centre de Recherches, d'Observation, de Secours et de Sauvetage (CROSS Corsen). For the densest part of the

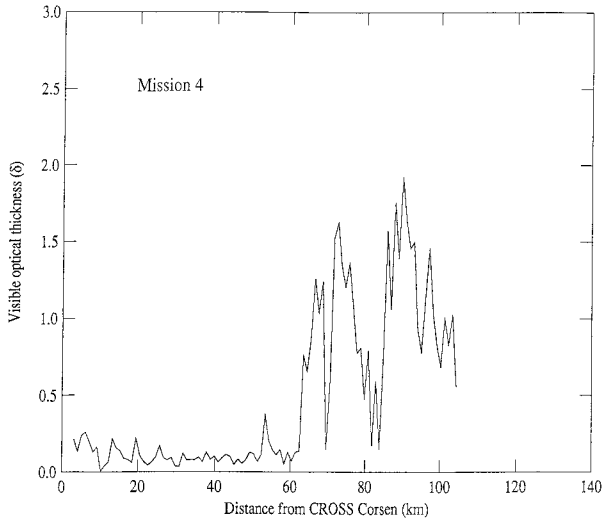

FIG. 11. Cirrus optical thicknesses at 532 nm obtained from the lidar LEANDRE along leg A1 during mission 4. For the densest part of the cloud (located between 50 and 100 km from CROSS Corsen), we have obtained a maximum value of 2 for the optical thickness.

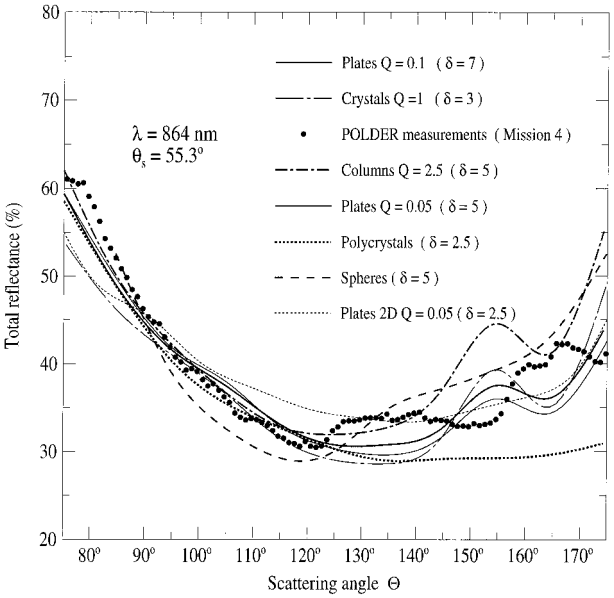

FIG. 12. Comparison of measurements of bidirectional total reflectance obtained by POLDER during mission 4 in the solar principal plane and modeling with different crystal shapes.

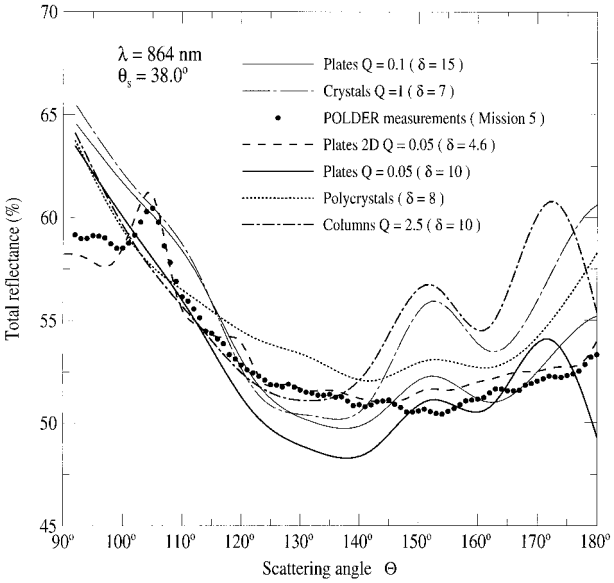

FIG. 13. Same as Fig. 12 but for mission 5.

cirrus cloud, located at a distance ranging between 85 and 88 km, δ is of the order of 2.

Bidirectional total reflectances were collected during missions 4 and 5 above the same homogeneous parts of cloud previously defined for the polarized bidirectional reflectances. Simulated bidirectional total reflectances, computed with the adding–doubling code and different microphysical models of randomly oriented particles, are compared to measurements in the solar principal plane. These results are presented in Fig. 12 as a function of the scattering angle. For mission 4, each type of randomly oriented particles could explain the measurements. None of them seems to give a better fit than any other, but the cloud optical thickness δ, necessary to obtain the best fit, is strongly dependent on the shape and the orientation of the particle, and ranges between 2.5 and 8. Note that theoretical results show oscillations for scattering angles greater than 120°. Indeed, the scattering phase function exhibits oscillations for scattering angles greater than 120°. Obviously these oscillations appear in single scattering and they remain, although attenuated, in multiple scattering. Concerning mission 5, measurements collected in the solar principal plane are presented in Fig. 13 as a function of the scattering angle. Oscillations are still observed for scattering angles greater than 120°, for the same reasons as in Fig. 12. The hot spot, observed for the zenithal viewing angle $\theta_v = \theta_s = 38°$, corresponds to the solar specular reflection. As for the previous case, different models were tested. The best fit is obtained for a cirrus cloud composed of horizontally oriented monocrystalline plates with an aspect ratio $Q = 0.05$ and an optical thickness $\delta = 5$. Because of their orientation, these plates are the only ones able to reproduce the specular reflection.

c. *Radiative flux measurements*

The upward and downward shortwave radiative fluxes measurements collected by pyranometers on board the Falcon led to the determination of the cloud plane albedo [Eq. (6)]. Figure 14 presents the plane albedo above cirrus cloud as a function of the distance from CROSS Corsen. When the aircraft flew over the densest part of

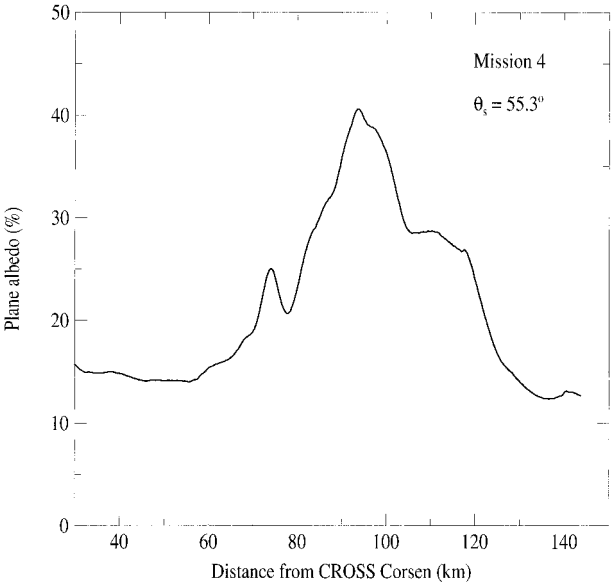

FIG. 14. Plane albedo measured with pyranometers on board the Falcon aircraft (mission 4) above cirrus cloud, as a function of distance from CROSS Corsen.

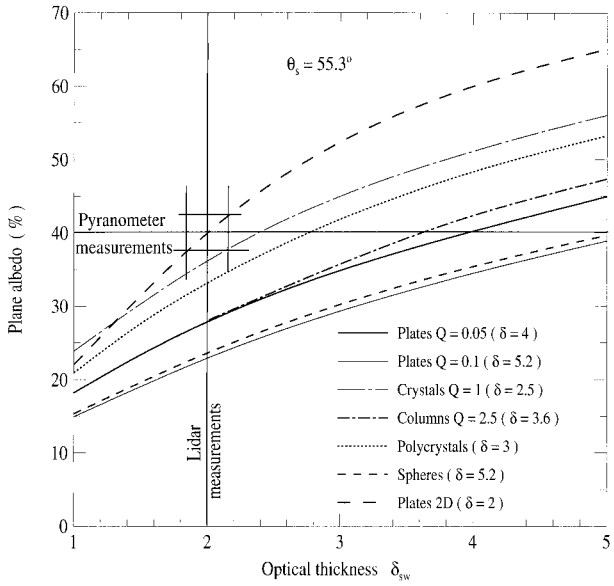

FIG. 15. Cirrus cloud plane albedo calculated for ice crystals randomly oriented in space (3D) and for plates horizontally oriented (2D). Optical thickness derived from lidar measurements and plane albedo derived from pyranometer measurements. For the optical thickness $\delta = 2$, only 2D-oriented plates are consistent with plane albedo measurements.

the cloud, the plane albedo reached a value of 40% with a relative uncertainty of about 10%. In Fig. 15, we present the calculated cloud plane albedo obtained for spatially and horizontally randomly oriented particles. For a given optical thickness and a solar zenith angle of the order of 55°, Fig. 15 shows an important variation of the cloud plane albedo with the microphysical model. This pointed out the impact of the microphysical model (i.e., the shape and the orientation of the particles) on the cirrus cloud at the scale of radiative transfer. In this case, the plane albedo can be increased by 50% when the plates are horizontally oriented, compared to the case where they are randomly oriented. Moreover, the impact of the orientation is certainly underestimated because of the approximation of random orientation that was used for high orders of scattering when we calculated the fluxes for the horizontally oriented particles. The measured value (40%) is reported in the same figure and shows that it can be explained by all the particles but for different optical thicknesses of the cirrus cloud ranging between 2 and 5.

7. Discussion and concluding remarks

We now discuss the coherence of the results obtained with different measurements, and see if one of the microphysical models described in this paper is able to satisfy all our observations.

The AVHRR measurements and the microphysical in situ probes are the only ones to provide information on particle size. For the observed cirrus cloud, the particle size corresponds to an effective radius of 20 μm for equivalent spheres.

We have conducted preliminary comparisons of reflectances and emissivities derived from AVHRR data with different simulations, using Henyey–Greenstein scattering functions. These comparisons show that thin and thick parts of the cirrus cloud seem to be composed of different kinds of ice crystals: a Henyey–Greenstein scattering function with asymmetry factor ranging between 0.7 and 0.8 seems to be able to reproduce AVHRR measurements collected above the thickest and densest part of the cloud.

Polarization measurements (POLDER bidirectional polarized reflectances and lidar linear depolarization ratio) have shown that spherical particles are not satisfactory to retrieve the cirrus cloud radiance field. We have used 3D randomly oriented prismatic particle models to explain polarization measurements, and our findings are as follows.

Randomly oriented (3D) prismatic particles are not able to satisfy the lidar linear depolarization ratio measured during mission 4. But Platt (1978), Elouragini (1991), and more recently Mishchenko et al. (1997) have pointed out that horizontally oriented (2D) particles show lower values of depolarization ratio than do the 3D-oriented ones. So a model of 2D-oriented particles could be able to reproduce linear depolarization measurements better than randomly oriented models.

Conclusions regarding the bidirectional polarized reflectances depend on the cirrus case studied. On the one hand, measurements collected during the morning (mission 4) can be explained with two types of 3D-oriented hexagonal plates ($Q = 0.05$ with $\delta = 1$, and $Q = 0.1$ with $\delta = 7$). On the other hand, measurements collected during the afternoon (mission 5) are well explained with cirrus cloud composed of polycrystals with an optical thickness of 8. Nevertheless, even if this microphysical model seems to be more conclusive than others, it is still unable to reproduce the specular reflection phenomenon.

Note that the model of 2D-oriented plates is not considered in explaining polarization measurements, because we have no radiative transfer code capable of computing polarization for such a medium.

For mission 4, measurements of backscattered to extinction ratio collected by the lidar can be explained with 3D-oriented plates (with a low value of aspect ratio Q) or with 2D-oriented particles. Shortwave optical thickness derived from lidar measurements is equal to 2 for the same sequence where the cloud is optically thick. This value is incoherent with an optical thickness of 1 or 7, which was obtained from simulations of polarized reflectances computed with the 3D-oriented plates. At the same time, bidirectional total reflectances measured by POLDER were compared with simulations for different shapes of prismatic crystals oriented in 2D or 3D. All of these simulations provide correct fits, but the optical thickness corresponding to each model is

Table 2. Results of comparisons between measurements and models. Here, (+) means that the model can explain measurements, (−) means that the model cannot explain measurements, (+/−) means that the model fits measurements better than other models but it does not correctly reproduce measurement, and (NC) means that the model and measurements have not been compared. Values given in parentheses correspond to cirrus cloud optical thickness that result in the best fit to measurements.

		Instrument	Plates $Q = 0.05$	Plates $Q = 0.1$	Crystals $Q = 1$	Columns $Q = 2.5$	Poly-crystals	Spheres $r = 20$ μm	Plates 2D
1	Plane albedo ($\theta_s = 55°$)	Pyranometers	+ (3.9)	+ (5.2)	+ (2.5)	+ (3.6)	+ (2.7)	+ (5.2)	+ (2)
2	Total reflectance ($\theta_s = 55°$)	POLDER	+ (5)	+ (7)	+ (3)	+ (5)	+ (2.5)	+ (8)	+ (2.5)
3	Backscatter to extinction ratio	Lidar	+	−	−	−	−	−	+/−
4	Polarized reflectance	POLDER	+ (1)	+ (7)	−	−	−	−	NC
5	Linear depolarization rate	Lidar	−	−	−	−	−	−	NC
6	Total reflectance and optical thickness	POLDER and lidar	−	−	−	−	+/− (2.5)	−	+/− (2.5)
7	Plane albedo and optical thickness	Pyranometers and lidar	−	−	+/− (2.5)	−	−	−	+ (2)
8	Total and polarized reflectances	POLDER	−	+ (7)	−	−	−	−	NC

highly variable. Optical thicknesses close to 2.5, in accordance with the lidar measurements, are obtained with 3D-oriented polycrystals and with 2D-oriented plates.

For mission 5, we do not have validated lidar optical thickness. Bidirectional total reflectances collected with POLDER were compared with simulations computed for each microphysical model. They show that horizontal plates are more appropriate than other crystal shapes because they are the only ones able to reproduce the specular reflection phenomenon. Moreover, Fig. 15, presented previously, shows that all microphysical models are able to explain the plane albedo measured during mission 4. But as the lidar optical thickness measured during this sequence was equal to 2, it shows that polycrystalline particles and horizontal plates are the only ones to simultaneously satisfy plane albedo measurements and measured lidar optical thickness. As polycrystalline particles were not able to satisfy the polarization measurement performed during the same sequence, we conclude that the 2D-oriented plates are the most representative particles. The results of the different comparisons between simulations and measurements collected during mission 4 are summarized in Table 2. Concerning the particles randomly oriented in space, we have limited our study to shape ratios ranging between 0.05 and 2.5, which are usually considered by many authors (Wendling et al. 1979; Takano and Liou, 1989b; Minnis et al. 1993):

The first part of Table 2 presents the results for each type of measurement considered alone. It appears that bidirectional total reflectance measurements and plane albedo measurements can be explained by every microphysical model, whereas polarization measurements are highly restrictive.

The second part of Table 2 presents various measurement combinations. Randomly oriented polycrystals and horizontally oriented plates can simultaneously reproduce bidirectional total reflectances and visible optical thickness from lidar, whereas 3D-oriented compact hexagonal particles ($Q = 1$) and 2D-oriented plates can explain both plane albedo and visible optical thickness from lidar. Randomly oriented plates ($Q = 0.1$) can explain both bidirectional total reflectances and bidirectional polarized reflectances.

Hence, none of the randomly oriented particles model is able to simultaneously reproduce the complete dataset collected during mission 4, and the only microphysical model that could be able to explain this dataset is the model of 2D-oriented plates.

Considering missions 4 and 5, we can conclude that for radiative measurements, the most appropriate microphysical model is the 2D-oriented plates. This conclusion is consistent with results obtained by several authors like Platt (1978), Sassen (1980), Lynch et al. (1994a,b), Shanks et al. (1995), and Mishchenko et al. (1997) who have pointed out the presence of 2D-oriented particles in cirrus clouds. But we have seen previously that the polarization has not yet been studied for 2D-oriented plates, because theoretical tools were not available. In fact there is currently no radiative transfer code able to calculate polarization for 2D-oriented plates. The adding–doubling code developed by Takano and Liou (1989b), as well as our approximated calculation used in this paper, do not include the polarization effect. Moreover, this conclusion regarding microphysical modeling of cirrus cloud observed on 17 April 1994 over Brittany has to be tested at the scale of the radiative budget. We have seen that for a solar zenith angle of the order of 55°, a cirrus cloud composed of 2D-oriented plates has a plane albedo increased by 50% compared to the case of a cirrus cloud composed of 3D-oriented plates. To observe the real impact of particle orientation on cloud radiative forcing, we have to know if the increase of plane albedo is important throughout the day,

that is, when the solar zenith angle is varying between 0° and 90°. This study will be presented in Part III of this series.

Acknowledgments. This work was supported by the European Community and European Space Agency under Contract EV5V-CT 92-0130 (EUCREX-2). The authors are very grateful to Y. Fouquart for the management of EUCREX-2, to A. Macke for providing the scattering matrix of polycrystals, to J. Hovenier and J. de Haan who gave us the opportunity to use their adding–doubling radiative transfer code, and to V. Giraud for his help concerning the analysis of AVHRR data. Thanks are also due to M. Tavet for correcting the English text and to the referees for their constructive remarks and comments.

REFERENCES

Allen, J. R., 1971: Measurements of cloud emissivity in the 8–13 μ waveband. *J. Appl. Meteor.,* **10,** 260–265.

Arnott, W. P., Y. Y. Dong, and J. Hallet, 1994: Role of small ice crystals in radiative properties of cirrus: A case study, FIRE II, November 22, 1991. *J. Geophys. Res.,* **99,** 1371–1381.

Brogniez, G., 1988: Light scattering by finite hexagonal crystals arbitrarily oriented in Space. *Proceedings of the International Radiation Symposium,* J. Lenoble and J. F. Geleyn, Eds., A. Deepak, 64–67.

——, F. Parol, J. C. Buriez, and Y. Fouquart, 1992: Bidirectional reflectances of cirrus clouds modelized from observations during the International Cirrus Experiment. *Proceedings of the International Radiation Symposium,* S. Keevallik and O. Karner, Eds., A. Deepak, 133–136.

Cai, Q., and K. N. Liou, 1982: Polarized light scattering by hexagonal crystals: Theory. *Appl. Opt.,* **21,** 3569–3580.

Cess, R. D., and Coauthors, 1990: Intercomparison and interpretation of climate feedback processes in 19 atmospheric general circulation models. *J. Geophys. Res.,* **95,** 16 601–16 615.

De Haan, J. F., P. B. Bosma, and J. W. Hovenier, 1986: The adding method for multiple scattering calculations of polarized light. *Astron. Astrophys.,* **183,** 371–391.

Deschamps, P. Y., F. M. Bréon, M. Leroy, A. Podaire, A. Brickaud, J. C. Buriez, and G. Sèze, 1994: The POLDER mission: Instrument characteristics and scientific objectives. *IEEE Trans. Geosci. Remote Sens.,* **32,** 598–615.

Deuzé, J. L., C. Devaux, M. Herman, R. Santer, and D. Tanré, 1988a: Saharan aerosols over the south of France: Characterization derived from satellite data and ground based measurements. *J. Appl. Meteor.,* **27,** 680–686.

——, M. Herman, and R. Santer, 1988b: Fourier series expansion of the transfer equation in the atmosphere–ocean system. *J. Quant. Spectrosc. Radiat. Transfer,* **41,** 483–494.

Elouragini, S., 1991: Etude des propriétés optiques et géométriques des cirrus par télédétection optique active (lidar) et passive (radiométrie). Ph.D. thesis, Université de Paris VI, 280 pp. [Available from Laboratoire de Météorologie Dynamique, Palaiseau, France.]

Giraud, V., J. C. Buriez, Y. Fouquart, F. Parol, and G. Sèze, 1997: Large-scale analysis of cirrus clouds from AVHRR data: Assessment of both a microphysical index and the cloud top temperature. *J. Appl. Meteor.,* **36,** 664–675.

Goloub, P., J. L. Deuzé, M. Herman, and Y. Fouquart, 1994: Analysis of the POLDER polarization measurements performed over cloud covers. *IEEE Trans. Geosci. Remote Sens.,* **32,** 78–88.

Hansen, J. E., A. Lacis, D. Rind, G. Russel, P. Stone, I. Fung, R. Ruedy, and J. Lerner, 1984: Climate sensitivity: Analysis of feedback mechanisms. *Climate Processes and Climate Sensitivity, Geophys. Monogr.,* No. 29, Amer. Geophys. Union, 130–163.

Heymsfield, A. J., 1975: Cirrus uncinus generating cells and the evolution of cirriform clouds. Part I: Aircraft measurements of the growth of the ice phase. *J. Atmos. Sci.,* **32,** 799–808.

——, 1977: Precipitation development in stratiform ice clouds: A microphysical and dynamical study. *J. Atmos. Sci.,* **34,** 367–381.

Inoue, T., 1985: On the temperature and the effective emissivity determination of semi-transparent cirrus clouds by bi-spectral measurements in the 10 μm window region. *J. Meteor. Soc. Japan,* **63,** 88–98.

Krupp, C., 1991: Holographic measurements of ice crystals in cirrus clouds during the International Cirrus Experiment ICE 1989. *Report of the 4th ICE/EUCREX Workshop,* R. W. Saunders and P. R. A. Brown, Eds., Meteorological Research Flight, 58–67.

Lenoble, J., 1993: *Atmospheric Radiative Transfer*. A. Deepak, 532 pp.

Liou, K.-N., 1986: Review. Influence of cirrus clouds on weather and climate processes: A global perspective. *Mon. Wea. Rev.,* **114,** 1167–1199.

Lynch, D. K., A. B. Fraser, and S. D. Gedzelman, 1994a: Subsuns, bottlinger's rings and elliptical halos. *Appl. Opt.,* **33,** 4580–4595.

——, J. G. Shanks, and S. D. Gedzelman, 1994b: Specular scattering and crystal dynamics in cirrus clouds. *Proc. SPIE/EOS Symp. on Passive Infrared Remote Sensing of Clouds and the Atmosphere,* Rome, Italy.

MacDowell, R. S., 1979: Frequency analysis of the circumzenithal arc: Evidence for the oscillations of ice crystals plates in the upper atmosphere. *J. Opt. Soc. Amer.,* **69,** 1119–1126.

Macke, A., J. Mueller, and E. Raschke, 1996: Single scattering properties of atmospheric ice crystal. *J. Atmos. Sci.,* **53,** 2813–2825.

Mie, G., 1908: Beigrade für Optik trufen Medien speziell kolloidaler Metallosungen. *Ann. Phys.,* **25,** 377–445.

Miloshevich, L. M., and A. J. Heymsfield, 1997: A balloon-borne continuous cloud particle replicator for measuring vertical profiles of cloud microphysical properties: Instrument design, performance, and collection efficiency analysis. *J. Atmos. Oceanic Technol.,* **14,** 753–768.

Minnis, P., K.-N. Liou, and Y. Takano, 1993: Inference of cirrus cloud properties using satellite-observed visible and infrared radiances. Part I: Parameterization of radiance fields. *J. Atmos. Sci.,* **50,** 1279–1304.

Mishchenko, M. I., D. J. Wielaard, and B. E. Carlson, 1997: T-matrix computations of zenith-enhanced lidar backscatter from horizontally oriented ice plates. *Geophys. Res. Lett.,* **24,** 771–774.

Mitchell, D. L., and W. P. Arnott, 1994: A model predicting the evolution of ice particles size spectra and radiative properties of cirrus clouds. Part II: Dependence of absorption and extinction on ice crystal morphology. *J. Atmos. Sci.,* **51,** 817–832.

Mitchell, J. N. F., C. A. Senior, and W. J. Ingram, 1989: CO_2 and climate: A missing feedback? *Nature,* **341,** 132–134.

Pelon, J., P. H. Flamant, and M. Meissonnier, 1990: The French airborne backscatter lidar LEANDRE-1: Concept and operation. *15th Int. Laser Radar Conf.,* Tomsk, USSR, Institute of Atmospheric Optics, 36–39.

Platt, C. M. R., 1973: Lidar and radiometric observations of cirrus clouds. *J. Atmos. Sci.,* **30,** 1191–1204.

——, 1978: Lidar backscatter from horizontal ice crystal plates. *J. Appl. Meteor.,* **17,** 482–488.

——, J. C. Scott, and A. C. Dilley, 1987: Remote sounding of high clouds. Part VI: Optical properties of midlatitude and tropical cirrus. *J. Atmos. Sci.,* **44,** 729–747.

Ramanathan, V., 1987: The role of the earth radiation budget studies in climate and general circulation research. *J. Geophys. Res.,* **92,** 4075–4095.

——, R. D. Cess, E. F. Harrison, P. Minnis, B. R. Bakstrom, E. Ahmad, and D. Hartmann, 1989: Cloud-radiative forcing and climate: Results from the Earth Radiation Budget Experiment. *Science,* **243,** 57–63.

Raschke, E., and K. D. Rockwitz, 1988: The International Cirrus Experiment. Some preliminary results from the first field phase. *Proceedings of the International Radiation Symposium*, J. Lenoble and J. F. Geleyn, Eds., A. Deepak, 6–9.

——, J. Schmetz, J. Heintzenberg, R. Kandel, and R. Saunders, 1990: The International Cirrus Experiment (ICE)—A joint European effort. *ESA J.*, **4,** 193–199.

Rockwitz, K. D., 1989: Scattering properties of horizontally oriented ice crystal columns in cirrus clouds. Part 1. *Appl. Opt.*, **28,** 4103–4110.

Sassen, K., 1980: Remote sensing of planar ice crystal fall attitudes. *J. Meteor. Soc. Japan*, **58,** 422–433.

——, 1991: The polarization lidar technique for cloud research: A review and current assessment. *Bull. Amer. Meteor. Soc.*, **72,** 1848–1866.

——, and N. C. Knight, 1994: Effects of ice-crystal structure on halo formation: Cirrus cloud experimental and ray-tracing modeling studies. *Appl. Opt.*, **33,** 4590–4601.

Saunders, R. W., G. Brogniez, J. C. Buriez, R. Meerkotter, and P. Wendling, 1992: A comparison of measured and modeled broadband fluxes from aircraft data during the ICE'89 field experiment. *J. Atmos. Oceanic Technol.*, **9,** 391–405.

Sauvage, L., H. Chepfer, V. Trouillet, P. H. Flamant, G. Brogniez, J. Pelon, and F. Albers, 1999: Remote sensing of cirrus radiative parameters during EUCREX'94: Case study of 17 April 1994. Part I: Observations. *Mon. Wea. Rev.*, **127,** 486–503.

Shanks, J. G., and D. K. Lynch, 1995: Specular scattering in cirrus cloud. *Infrared Remote Sensing of Clouds and Atmosphere III, Proc. EROPTO Series*, Paris, France, SPIE, Vol. 2578, 227–238.

Slingo, A., and H. M. Schrecker, 1982: On the shortwave radiative properties of stratiform water clouds. *Quart. J. Roy. Meteor. Soc.*, **108,** 407–426.

Takano, Y., and K. N. Liou, 1989a: Solar radiative transfer in cirrus clouds. Part I: Single-scattering and optical properties of hexagonal ice crystals. *J. Atmos. Sci.*, **46,** 3–19.

——, and ——, 1989b: Solar radiative transfer in cirrus clouds. Part II: Theory and computation of multiple scattering in an anisotropic medium. *J. Atmos. Sci.*, **46,** 20–36.

van de Hulst, H. C., 1981: *Light Scattering by Small Particles.* Dover, 470 pp.

Wendling, P., R. Wendling, and H. K. Weickmann, 1979: Scattering of solar radiation by hexagonal ice crystals. *Appl. Opt.*, **18,** 2663–2671.

Wetherald, R. T., and S. Manabe, 1988: Cloud feedback processes in a general circulation model. *J. Atmos. Sci.*, **45,** 1397–1415.

Wielicki, B. A., and Coauthors, 1990: The 27–28 October 1986 FIRE IFO cirrus case study: Comparison of radiative transfer theory with observations by satellite and aircraft. *Mon. Wea. Rev.*, **118,** 2356–2376.

Woodbury, G. E., and P. Mc Cormick, 1986: Zonal and geographycal distributions of cirrus clouds determined from SAGE data. *J. Geophys. Res.*, **91,** 2775–2785.